EDGE ARTICLE

Check for updates

Highly efficient visible-light photocatalytic ethane oxidation into ethyl hydroperoxide as a radical reservoir†

Yao Zhu,‡[a] Siyuan Fang,‡[b] Shaoqin Chen,[a] Youjie Tong,[a] Chunling Wang[a] and Yun Hang Hu ⓘ ★[ab]

Photocatalytic ethane conversion into value-added chemicals is a great challenge especially under visible light irradiation. The production of ethyl hydroperoxide (CH_3CH_2OOH), which is a promising radical reservoir for regulating the oxidative stress in cells, is even more challenging due to its facile decomposition. Here, we demonstrated a design of a highly efficient visible-light-responsive photocatalyst, Au/WO_3, for ethane oxidation into CH_3CH_2OOH, achieving an impressive yield of 1887 $\mu mol\ g_{cat}^{-1}$ in two hours under visible light irradiation at room temperature for the first time. Furthermore, thermal energy was introduced into the photocatalytic system to increase the driving force for ethane oxidation, enhancing CH_3CH_2OOH production by six times to 11 233 $\mu mol\ g_{cat}^{-1}$ at 100 °C and achieving a significant apparent quantum efficiency of 17.9% at 450 nm. In addition, trapping active species and isotope-labeling reactants revealed the reaction pathway. These findings pave the way for scalable ethane conversion into CH_3CH_2OOH as a potential anticancer drug.

Introduction

Ethane, as the second abundant constituent of natural gas (~10%) and one of the major pollutants emitted from both biogenic and anthropogenic sources (~9.57 Tg per year), can be utilized to produce value-added chemical substances such as ethanol, acetaldehyde, acetic acid, ethylene, and hydrochloric ether.[2–4] Although ethyl hydroperoxide (CH_3CH_2OOH) could be generated in ethane oxidation, it is generally regarded as an intermediate species due to its facile decomposition.[5,6] However, the synthesis of CH_3CH_2OOH is very attractive because it is a reservoir for both reactive oxygen species (ROS) such as HO_x radicals and $^1O_2$, and some carbon-containing free radicals such as alkyl, alkyloxy, and alkylperoxyl radicals.[6–9] In the presence of a trace amount of enzyme, hematin, or some metal ions, these active species can be released by CH_3CH_2OOH to regulate the oxidative stress in the cell, as a promising approach for cancer therapy.[7–13] This will even outperform the present photodynamic therapy techniques that are highly dependent on the oxygen and external light.[13–15] Thus, achieving

the stable conversion of ethane into CH_3CH_2OOH is highly desirable.

Compared with traditional catalytic processes, photocatalytic ethane conversion is much more intriguing because it can take place under a milder condition with a lower cost.[1,16–25] So far, TiO_2, ZnO, CeO_2, MoO_3, and V_2O_5 have been explored as the photocatalysts for ethane oxidation,[22–26] but only UV light can be absorbed due to their large band gaps. However, in the solar irradiation spectrum, UV light accounts for only 3%, while visible light constitutes 44%.[27,28] Thus, it is highly expected to develop visible-light-responsive photocatalysts for ethane oxidation. Here, WO_3 is a promising candidate with a narrow band gap (2.4–2.8 eV) and a high resistance to photo-corrosion.[29,30] Nevertheless, pure WO_3 generally shows a high charge carrier recombination rate, requiring modifications such as loading cocatalysts, introducing dopants, and adjusting morphologies.[31–33] Modified WO_3 has been successfully applied in water splitting, pollutant degradation, and solar energy conversion,[34,35] and is desirable to achieve efficient ethane oxidation under visible light irradiation. This is the first hypothesis of the present work.

Being able to absorb visible light cannot ensure the effective utilization of visible light to drive corresponding redox reactions. For example, Pt-loaded black TiO_2 could absorb visible light, but it exhibited a negligible activity for water splitting under visible light irradiation.[36] Here, as revealed in our previous work, though a narrow band gap of the photocatalyst allows visible light absorption, it meanwhile causes the insufficient driving force for the redox reactions, resulting in a poor

[a]School of Environmental Science and Engineering, Shanghai Jiao Tong University, Shanghai 200240, China

[b]Department of Materials Science and Engineering, Michigan Technological University, Houghton, Michigan 49931, USA. E-mail: yunhangh@mtu.edu

catalytic performance.[37] The introduction of thermal energy into the photocatalytic system, as a novel thermo-photo catalytic approach, can effectively address this issue. This is because the kinetic energy of the reactants increased by the temperature rise can compensate the potential driving force for corresponding redox reactions. As a result, the visible-light driven photocatalytic activities were significantly improved in a series of chemical processes including water splitting,[37–39] CO_2 reforming of CH_4,[40] steam reforming of CH_4,[41] CO hydrogenation,[42] and CO_2 hydrogenation.[43] Based on our previous successes, introducing thermal energy is expected to enhance the efficiency of ethane oxidation under visible light irradiation, which constitutes the second hypothesis of this work.

On top of these two hypotheses, revealing the reaction pathway of photocatalytic ethane oxidation is even more essential. On the one hand, multiple products with various oxidation degrees might be generated in ethane oxidation. Elucidating the reaction pathway will help to exploit the strategies to enhance the selectivity for the desirable product. On the other hand, identifying the roles of each reactants (e.g., oxygen and water) will contribute to the exploration of approaches to accelerate the reaction. So far, only a few efforts have been made, mainly based on the results of nuclear magnetic resonance spectroscopy,[44] in situ infrared spectroscopy and trapping active species,[25,45] whereas the solid and comprehensive investigation into the reaction mechanism has not been conducted yet.

In this work, Au/WO_3 was designed and synthesized as a visible-light-responsive photocatalyst for visible-light driven photocatalytic ethane oxidation in the presence of oxygen and water. An impressive yield of CH_3CH_2OOH (1887 μmol g_{cat}^{-1}) was obtained in the two-hour visible-light driven photocatalytic process at room temperature for the first time, which was further enhanced by six times via elevating the reaction temperature to 100 °C, with a high selectivity of 63.6% and an apparent quantum efficiency up to 17.9% at 450 nm. More importantly, the synergistic roles of the Au/WO_3 catalyst, visible light irradiation, and thermal energy in efficient ethane oxidation into CH_3CH_2OOH, as well as the comprehensive reaction mechanism of ethane conversion, were uncovered.

Results and discussion

Design and synthesis of Au/WO_3 as a visible-light-responsive catalyst

There are three requirements for designing an efficient photocatalyst. First, the band structure of the catalyst must match the redox potentials of the desirable reaction. Second, it can absorb as much light as possible. Third, photo-generated electrons and holes can be effectively separated to drive corresponding redox reactions. In this light, to create an ideal catalyst for ethane oxidation, we selected WO_3 as an active component due to its narrow band gap for visible light response and Au as a promoter since it can not only assist charge transfer but also enhance light harvest due to the surface plasmon resonance (SPR) effect.[30,46]
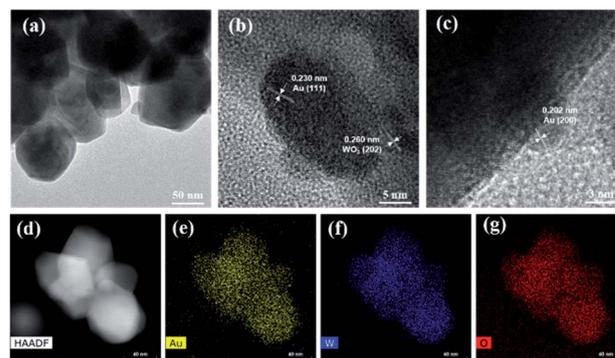

Fig. 1 TEM images of Au/WO_3. (a) TEM image. (b) and (c) HRTEM images. (d) HAADF-STEM image. (e) Au element EDX map. (f) W element EDX map. (g) O element EDX map.

Au/WO_3 was prepared by photo-depositing Au onto monoclinic WO_3 nanoparticles. The Au loading amount was 0.33 wt% as determined by ICP-MS. In spite of the small loading amount, a weak peak corresponding to metallic Au (at 38.337°) was observed in the XRD pattern (Fig. S1†).[47] The morphological structure of Au/WO_3 is shown in Fig. 1a, where Au nanoparticles with an average size of ∼16 nm dispersed on the surface of WO_3 (see Fig. S2† for the size distribution of Au). Moreover, the d-spacings of lattice fringes of 0.260, 0.230, and 0.202 nm were recognized (Fig. 1b and c), attributed to WO_3(202), Au(111), and Au(200), respectively.[47,48] Furthermore, elemental mapping (Fig. 1d–g) revealed the uniform distribution of Au, W, and O. The BET surface area and the BJH average pore diameter and volume of this catalyst were determined as 4.51 m^2 g^{-1}, 262 Å, and 0.0368 cm^3 g^{-1}, respectively (Fig. S3†). In addition, both lattice oxygen (O^{2-}) and adsorbed oxygen (O^- and O_2^-) were observed in the O 1s XPS spectrum (Fig. S4a†),[48] while W existed in the +6 state with the peaks for W $4f_{7/2}$ and W $4f_{5/2}$ shifted to higher values compared with those for pure WO_3, indicating the strong interaction between Au and WO_3 (Fig. S4b†). The Au 4f XPS spectrum of the catalyst was just the same as the standard one of metallic Au (Fig. S4c†).[47]

The UV-vis absorption spectra of Au/WO_3 and WO_3 are shown in Fig. 2a. Compared with WO_3, Au/WO_3 showed an enhanced light absorption from 450 to 700 nm with an absorption peak at 550 nm, owing to the SPR effect of Au nanoparticles.[46] The band gap of Au/WO_3 was then calculated to be 2.43 eV, enabling a visible-light driven photocatalytic process. To ensure that the thermodynamic requirements are satisfied, the band structure of Au/WO_3 was analysed as following. The Mott–Schottky plots (Fig. S5†) indicated that the Fermi level locates at 0.71 V (vs. NHE) while the valence-band XPS spectrum (Fig. S4d†) showed a main absorption onset at 1.51 eV, by which the valence band maximum was estimated to be 2.22 V (vs. NHE). Considering the band gap of 2.43 eV, the conduction band minimum was then obtained as −0.21 V (vs. NHE). Thereby, the band structure of Au/WO_3 was depicted in Fig. 2b, consistent with reported ones.[46,49]

Here, a series of reduction reactions would take place with photo-generated electrons, forming $^•O_2^-$, H_2O_2, and $^•OH$. The
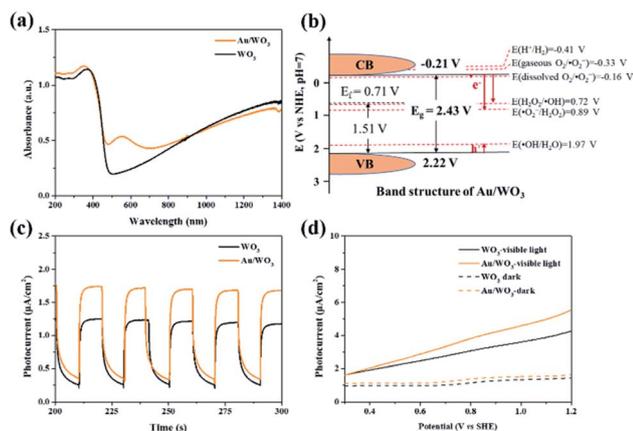
Fig. 2 Optical and photoelectric properties of the catalyst. (a) UV-visible absorption spectra of Au/WO₃ and WO₃. (b) Band structure of Au/WO₃ and redox potentials of possible reactions. (c) Photocurrent–time curves of Au/WO₃ and WO₃. (d) Linear sweep voltammetry curves of Au/WO₃ and WO₃.

reduction of gas-phase O_2 cannot happen since its redox potential (-0.33 V *vs.* NHE) is above the conduction band minimum, but dissolved O_2 can be reduced with a favorable redox potential of -0.16 V *vs.* NHE.[50–52] This implies the vital importance of carrying out ethane oxidation in an aqueous condition. Moreover, owing to this unique band structure, the reduction of H^+ into H_2 is inhibited, effectively enhancing the production of above oxidizing agents. Meanwhile, photo-generated holes could oxidize water with ˙OH as the byproduct. The formation of these ROS would make a great contribution to ethane oxidation.

Moreover, Au/WO₃ showed a high efficiency for separating photo-generated electrons and holes as demonstrated by its stable photocurrent of 1.74 μA cm⁻² under visible light irradiation, which was much higher than that of WO₃ (1.23 μA cm⁻²) (Fig. 2c). This agreed well with the result of linear sweep voltammetry (Fig. 2d), namely, enhanced current density was acquired on Au/WO₃ compared with that of WO₃. Therefore, the aforementioned three requirements for designing a high-performance photocatalyst are met, highlighting the great

Table 1 Reported photocatalytic activities of ethane oxidation

Catalyst	Oxidant	Light	Pressure	Temp.	Yield (μmol g_{cat}^{-1} h^{-1})	Ref.
ZnO	O_2	UV	Gas flow with C_2H_6 : O_2 : He of 3 : 1 : 10	220 °C	336 (CH_3CHO) 280 (CO_2) 28 (CO) 24 (HCHO) 11 (CH_3CH_2OH)	1
MoO₃/SiO₂	O_2	UV	Gas flow with C_2H_6 : O_2 : He of 3 : 1 : 10	220 °C	2400 (CH_3CHO) 880 (HCHO) 200 (CO_2) 92 (CH_3CH_2OH)	19
BiOX-POM	O_2	UV + visible (cold white LED lamp)	Gas flow with C_2H_6 : O_2 of 1 : 1	RT	72 (CH_3CHO)	20
V₂O₅/SiO₂	O_2	UV	Gas flow with C_2H_6 : O_2 : He of 3 : 1 : 10	220 °C	2480 (CH_3CHO) 280 (HCHO) 80 (CO_2) 40 (CO)	21
Au/TiO₂	H_2O	UV, 59 mW cm⁻²	Gas flow with C_2H_6 : H_2O : Ar of 1 : 1 : 8	RT	0.07 (CO_2)	22
Pd–MoO₃/SiO₂	CO_2	UV, 40 mW cm⁻²	Gas flow with C_2H_6 : CO_2 of 1 : 1	150 °C	28 (CH_3CHO) 5 (C_2H_5CHO) 3 (CH_3CH_2OH) 4 (CH_3CHO) 3 (CO)	23
ZnO–TiO₂/SiO₂	CO_2	UV, 40 mW cm⁻²	Gas flow with C_2H_6 and CO_2	200 °C	25 (C_2H_5CHO) 8 (C_4H_{10}) 4 (CH_3CHO) 3 (CO)	24
Pd/TiO₂	CO_2	UV	0.1 MPa C_2H_6 and 0.1 MPa CO_2/Ar	RT	231 (C_2H_4) 118 (CO) 22 (CH_4)	25
Au/WO₃	O_2	Visible (λ >420 nm), 100 mW cm⁻²	1.0 MPa 4 : 1 C_2H_6/N_2 and 1.5 MPa O_2	RT	944 (CH_3CH_2OOH) 311 (CH_3CHO) 293 (CH_3COOH)	This work
				100 °C	5617 (CH_3CH_2OOH) 1799 (CH_3CHO) 665 (CH_3COOH) 449 (CH_3CH_2OH)	This work

promise of Au/WO$_3$ as a highly efficient photocatalyst for ethane oxidation under visible light irradiation.

Visible-light driven photocatalytic ethane oxidation over Au/WO$_3$

As shown in Fig. S6,† photocatalytic ethane oxidation was carried out in a sealed reactor under visible light irradiation (λ >420 nm, 100 mW cm^{-2}). Besides ethane and oxygen, water was also introduced into the reactor to dissolve oxygen to enable a thermodynamically favorable photocatalytic process. As expected, the two-hour room-temperature photocatalytic reaction over Au/WO$_3$ catalyst (35 °C as measured by the thermocouple) resulted in an impressive yield of CH$_3$CH$_2$OOH (1887 μmol g$_{cat}^{-1}$), together with some CH$_3$CHO (621 μmol g$_{cat}^{-1}$) and CH$_3$COOH (585 μmol g$_{cat}^{-1}$), surpassing current reports (at room temperature) even though their yields were obtained under UV light or simulated sunlight irradiation (Table 1).

Here, considering the intrinsic issue of visible-light photocatalysis, namely, the contradiction between visible light absorption and sufficient driving force, we propose that the introduction of thermal energy, which can help to break the kinetic limitation of the reaction, will greatly promote ethane oxidation under visible light irradiation. By analysing the band structure of Au/WO$_3$, the driving forces for O$_2$ reduction (*i.e.*, energy difference between the redox potential of dissolved O$_2$/˙O$_2^-$ and the conduction band minimum) and H$_2$O oxidation (*i.e.*, energy difference between the redox potential of ˙OH/H$_2$O and the valence band maximum) were found as small as 0.05 and 0.25 V, respectively. The introduction of thermal energy by simply increasing the reaction temperature will enhance the kinetic energy of the reactants, thus providing additional kinetic driving force for the semi-reactions. The compensation effect of the kinetic driving force with regards to the potential driving force is highly expected to lead to highly efficient ethane oxidation under visible light irradiation.

To demonstrate above hypothesis, photocatalytic ethane oxidation was carried out at 50, 100, 150, 180, and 200 °C. The results are shown in Fig. 3a, where the yield of CH$_3$CH$_2$OOH reached 11 233 μmol g$_{cat}^{-1}$ at 100 °C, which was six times of that obtained at room temperature. The production of CH$_3$CHO and CH$_3$COOH was also enhanced, with a new high-value product, CH$_3$CH$_2$OH, being obtained. These products were further evidenced by ^{1}H NMR (Fig. S7†) and GC-MS (Fig. S8–S11†). The significant production efficiencies outperform not only all the reported values (Table 1), but also those obtained with other catalysts under the same test condition (Fig. S12†), indicating the superiority of the Au/WO$_3$ catalyst. Herein, Au contributed to both charge separation and light harvest due to SPR as demonstrated by the fact that loading other metals without evident SPR effect showed much poorer efficiencies. However, although the increase of the Au loading amount from 0.08 to 0.33 wt% promoted ethane oxidation, excessive Au loading of 0.69 wt% resulted in the decreased yield (Fig. S13†) because Au nanoparticles could also act as the recombination centers of electrons and holes.[53,54] Furthermore, different from other reports with CH$_3$CHO as the major product, the selectivity of CH$_3$CH$_2$OOH we obtained was as high as 63.6%, marking an effective way to produce such an easy-to-decompose substance which is promising for cancer therapy. As-produced liquid could be further purified by column chromatography, *etc.*, for further application. The apparent quantum efficiency over Au/WO$_3$ at 100 °C was measured as high as 17.9% at 450 nm, again demonstrating the excellent ethane oxidation performance achieved by thermo-photo catalysis. The decrease of the yield in the temperature range from 150 to 200 °C was due to the overoxidation of ethane into CO$_2$ and the decreased solubility of feed gases, which were supported by the enhanced CO$_2$ yield and lowered total yield, respectively.

In contrast, as shown in Fig. 3b, in the process at 100 °C without illumination, negligible oxidation products were detected, evidencing the little contribution of thermal catalysis to ethane oxidation at this temperature. In addition, the activity under simulated sunlight irradiation (AM1.5G) was just slightly higher than that obtained under visible light irradiation, indicating that the activity of ethane oxidation was directly correlated to photo energy (as distributed by light wavelengths). Furthermore, light irradiation with wavelengths above 510 nm resulted in very low yields of ethane oxidation products because these lights cannot be absorbed by Au/WO$_3$ (with a band gap of 2.43 eV) to generate electrons and holes. This also implied the very limited contribution of hot electrons of Au derived from the plasmonic effect to ethane oxidation. These observations demonstrated that ethane oxidation under illumination at 100 °C still followed a photocatalytic pathway. Therefore, our hypothesis (that the introduction of thermal energy can accelerate the photocatalytic process of ethane oxidation under visible light irradiation by enhancing the driving force) was exactly confirmed.

Water plays a key role in photocatalytic ethane oxidation since negligible product was detected in the reaction without
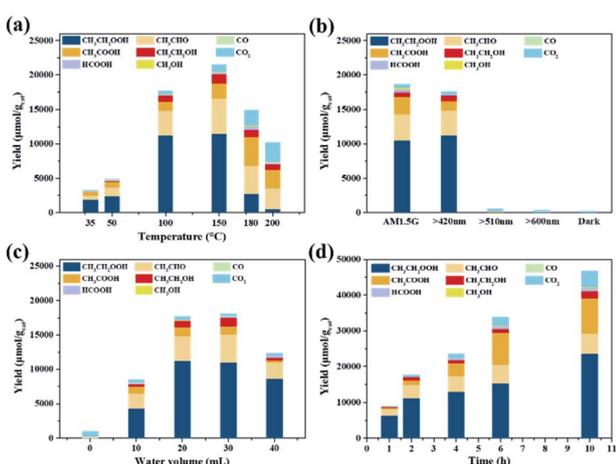

Fig. 3 Photocatalytic ethane oxidation over Au/WO$_3$. (a) Visible-light driven ethane oxidation at various temperatures (reacting for 2 h in 20 mL water). (b) Ethane oxidation under various lights (reacting for 2 h in 20 mL water at 100 °C). (c) Visible-light driven ethane oxidation with various water volumes (reacting for 2 h at 100 °C). (d) Visible-light driven ethane oxidation with various reaction times (in 20 mL water at 100 °C).
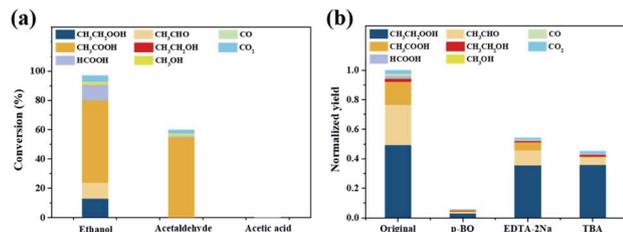
Fig. 4 Identification of the reaction pathway and active species in visible-light driven photocatalytic ethane oxidation over Au/WO_3. (a) Conversion efficiency using ethanol, acetaldehyde, or acetic acid as the reactant. (b) Normalized yield obtained with the employment of trapping agents.

water (Fig. 3c). Besides enabling a process with dissolved O_2 as the reduced species to meet the thermodynamic requirement of photocatalysis, water also accelerates ethane oxidation via the following two aspects. On the one hand, water is the source of some ROS such as $^{\cdot}OH$ and H_2O_2. On the other hand, water could serve as an effective solvent for the oxidation products, cleaning the catalyst surface and regenerating the active sites. Both aspects could be promoted at an appropriately elevated temperature due to the enhanced water dissociation (to form OH^- which can be oxidized into $^{\cdot}OH$ more easily) and the accelerated desorption of the products. However, excessive amount of water led to the decrease of the yield, because in such a three-phase system, the contact between the feed gases and catalyst could be suppressed by water. The prolongation of the reaction from 2 to 10 hours showed a nearly linear enhancement in ethane oxidation (Fig. 3d), indicating there was no evident photo-corrosion. However, the time extension mainly promoted the overoxidation into CH_3COOH and CO_2 while lowered the selectivity of CH_3CH_2OOH. Thus, considering the time effectiveness, activity, and selectivity, two-hour reaction was the best.

Reaction pathway

Since multiple oxidation products with various oxidation degrees were detected, visible-light driven ethane oxidation over Au/WO_3 is highly possible to undergo a stepwise process. When using CH_3CH_2OH as the reactant, its conversion efficiency was as high as 96.9%, generating the same types of products as those obtained from ethane oxidation (Fig. 4a), indicating that CH_3CH_2OH was an important intermediate species. The major product was CH_3COOH, while the generation of CH_3CH_2OOH, as the most abundant and desirable product, showed a poor selectivity of 13.2% (much below that of 63.6% in ethane oxidation), suggesting that CH_3CH_2OH might not be the main

intermediate to CH_3CH_2OOH. Besides, the conversion efficiency of CH_3CHO was just 60.0%, with CH_3COOH as the dominant product with a high selectivity of 91.3%, revealing that CH_3CHO was a key intermediate to CH_3COOH. Only minor amount of CH_3COOH could be further converted. Above results implied CH_3CH_2OOH was not mainly produced from CH_3CH_2OH, CH_3CHO, and CH_3COOH, but, as a primary product directly generated from ethane.[3,44]

Moreover, to reveal the role of active species in photocatalytic ethane oxidation, trapping agents, including p-benzoquinone (p-BQ), tertiary butyl alcohol (TBA), and ethylenediaminetetraacetic acid disodium salt dihydrate (EDTA–2Na), were employed to trap $^{\cdot}O_2^-$, $^{\cdot}OH$, and holes, respectively. A small addition of p-BQ (10 mM) led to a 94.4% decrease in the total yield (Fig. 4b), indicating the vital importance of $^{\cdot}O_2^-$. In the photocatalytic reduction semi-reaction, $^{\cdot}O_2^-$ was first produced, by which H_2O_2 and $^{\cdot}OH$ could be formed successively. Therefore, trapping $^{\cdot}O_2^-$ would result in an evident decrease of ROS and thereby a low yield. Moreover, $^{\cdot}O_2^-$ played a key role for generating CH_3CH_2OOH, which would be revealed in the following part. In contrast, the effect induced by trapping holes was smaller, causing a 45.6% decrease of the total yield. As proposed in Fig. 2b, holes would react with H_2O to form $^{\cdot}OH$, which could then contribute to ethane oxidation. Even though holes were trapped, $^{\cdot}OH$ could still be produced from the reduction semi-reaction, thus the influence on the yield was not very much noticeable. Moreover, by trapping $^{\cdot}OH$, the production of CH_3CH_2OOH was slightly affected while the yields of CH_3CHO and CH_3COOH significantly decreased, indicating that $^{\cdot}OH$ is directly correlated to the formation of CH_3CHO and CH_3COOH but not CH_3CH_2OOH.

Furthermore, isotope labeling experiments with the use of O^{18}_2, H_2O^{18}, or D_2O, were conducted to demonstrate the origin of each product. The products detected by GC-MS are shown in Table 2 (see Fig. S8–S11† for the GC-MS spectra). Employing O^{18}_2 resulted in the formation of $CH_3CH_2O^{18}O^{18}H$, $CH_3CH_2O^{18}H$, CH_3CHO^{18}, $CH_3CO^{18}O^{18}H$, $CH_3CO^{18}OH$, and $CH_3COO^{18}H$, while the use of H_2O^{18} generated CH_3CHO^{18}, $CH_3CO^{18}O^{18}H$, $CH_3CO^{18}OH$, and $CH_3COO^{18}H$. Moreover, replacing general water by D_2O made the hydroperoxyl group of CH_3CH_2OOH be fully deuterated and the carboxy group of CH_3COOH be partially deuterated.

According to the above results, the reaction pathway was proposed as following. First of all, visible light was absorbed by Au/WO_3 to generate active electrons and holes (eqn (1)). Considering the thermodynamic requirements of photocatalysis (Fig. 2b), photo-generated electrons would transfer from the conduction band of WO_3 to Au nanoparticle to reduce dissolved O_2 into $^{\cdot}O_2^-$ (eqn (2)), which could be further

Table 2 Products obtained in isotope labeling experiments

Reactant	CH_3CH_2OOH	CH_3CH_2OH	CH_3CHO	CH_3COOH
O^{18}_2	$CH_3CH_2O^{18}O^{18}H$	$CH_3CH_2O^{18}H$	CH_3CHO^{18}	$CH_3CO^{18}O^{18}H$, $CH_3CO^{18}OH$, $CH_3COO^{18}H$ and CH_3COOH
H_2O^{18}	CH_3CH_2OOH	CH_3CH_2OH	CH_3CHO^{18}	$CH_3CO^{18}O^{18}H$, $CH_3CO^{18}OH$, $CH_3COO^{18}H$ and CH_3COOH
D_2O	CH_3CH_2OOD	CH_3CH_2OH	CH_3CHO	CH_3COOD and CH_3COOH

converted into H_2O_2 (eqn (3)) and $^{\bullet}OH$ (eqn (4)), while photo-generated holes remaining on WO_3 would oxidize H_2O into $^{\bullet}OH$ (eqn (5)).

$$Au/WO_3 + h\nu \rightarrow e^- + h^+ \tag{1}$$

$$O_2 + e^- \rightarrow {}^{\bullet}O_2^- \tag{2}$$

$${}^{\bullet}O_2^- + 2H^+ + e^- \rightarrow H_2O_2 \tag{3}$$

$$H_2O_2 + H^+ + e^- \rightarrow {}^{\bullet}OH + H_2O \tag{4}$$

$$H_2O + h^+ \rightarrow {}^{\bullet}OH + H^+ \tag{5}$$
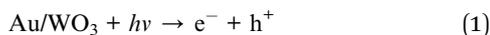
CH_3CH_3 could react with either h^+ (eqn (6)) or $^{\bullet}OH$ (eqn (7)) to form an unstable intermediate radical $CH_3CH_2^{\bullet}$.[25] The participation of both h^+ and $^{\bullet}OH$ was supported by the result of trapping experiments, namely, trapping h^+ or $^{\bullet}OH$ did not completely inhibit the reaction. $^{\bullet}O_2^-$ could be protonated by H^+ in water to generate $^{\bullet}OOH$ (eqn (8)),[55,56] which then reacted with $CH_3CH_2^{\bullet}$ to form CH_3CH_2OOH (eqn (9)). Since $^{\bullet}OOH$ and $CH_3CH_2^{\bullet}$ were generated on Au and WO_3 respectively, the most favourable site for CH_3CH_2OOH production was the interface of Au and WO_3. Such a pathway for CH_3CH_2OOH production agreed well with the result of isotope labeling experiments, namely, the O atoms in CH_3CH_2OOH were from O_2 while the H atom in the hydroperoxyl group originated from water. The insertion of $^{\bullet}O_2^-$ was the preliminary step for the generation of subsequent oxidation products, thus trapping $^{\bullet}O_2^-$ led to a sharp drop of the yields (Fig. 4b).

$$CH_3CH_3 + h^+ \rightarrow CH_3CH_2^{\bullet} + H^+ \tag{6}$$

$$CH_3CH_3 + {}^{\bullet}OH \rightarrow CH_3CH_2^{\bullet} + H_2O \tag{7}$$

$${}^{\bullet}O_2^- + H^+ \rightarrow {}^{\bullet}OOH \tag{8}$$

$$CH_3CH_2^{\bullet} + {}^{\bullet}OOH \rightarrow CH_3CH_2OOH \tag{9}$$

Since the O atom in CH_3CH_2OH came from O_2 rather than H_2O, it was most likely to be resulted with CH_3CH_2OOH as the intermediate as shown in eqn (10) and (11). Here, eqn (11) ensured that H_2O was not the source of the H atom in the hydroxy group. Eqn (10) and (11) could proceed reversibly because CH_3CH_2OOH was detected as one of the products in photocatalytic conversion of CH_3CH_2OH (Fig. 4a).

$$CH_3CH_2OOH \rightleftharpoons CH_3CH_2O^{\bullet} + {}^{\bullet}OH \tag{10}$$

$$CH_3CH_2O^{\bullet} + CH_3CH_3 \rightleftharpoons CH_3CH_2OH + CH_3CH_2^{\bullet} \tag{11}$$

CH_3CHO could be produced either from CH_3CH_2OH (eqn (12)) or directly from CH_3CH_2OOH (eqn (13)), by which the O atom in CH_3CHO originated from O_2. Moreover, the detected CH_3CHO^{18} with H_2O^{18} as the reactant was ascribed to the reversible reaction between CH_3CHO and $CH_3CH(OH)_2$ (eqn (14)). The existence of $CH_3CH(OH)_2$ was evidenced by ^1H NMR spectrum (Fig. S7†). In this case, both H atoms and at least one O atom(s) in the hydroxyl groups of $CH_3CH(OH)_2$ should be derived from H_2O.

$$CH_3CH_2OH + 2{}^{\bullet}OH \rightarrow CH_3CHO + 2H_2O \tag{12}$$

$$CH_3CH_2OOH \rightarrow CH_3CHO + H_2O \tag{13}$$

$$CH_3CHO + H_2O \rightleftharpoons CH_3CH(OH)_2 \tag{14}$$

$CH_3CH(OH)_2$ could be further oxidized into CH_3COOH by $^{\bullet}OH$ (eqn (15)), in which the H atom and at least one O atom(s) in the carboxy group originated from H_2O, partially agreeing with the result of isotope labeling experiments (Fig. S11d†). Thus, there should be another pathway leading to the formation of CH_3COOH in which both O atoms came from O_2 and the H atom in the carboxy group was not derived from H_2O. This might be achieved via eqn (16) and (17).

$$CH_3CH(OH)_2 + 2{}^{\bullet}OH \rightarrow CH_3COOH + 2H_2O \tag{15}$$

$$CH_3CH_2OH + 2{}^{\bullet}OOH \rightarrow CH_3CH(OOH)(OH) + H_2O_2 \tag{16}$$

$$CH_3CH(OH)(OOH) \rightarrow CH_3COOH + H_2O \tag{17}$$
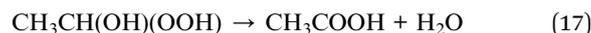
The cleavage of the C–C bond occurred in CH_3CH_2OH and CH_3CHO because HCOOH and CH_3OH were detected after photocatalytic oxidation of CH_3CH_2OH and CH_3CHO (Fig. 4a). The production of HCOOH from CH_3CH_2OH was proposed via eqn (18) and (19), with the assistance of $^{\bullet}OH$. HCOOH could also be resulted by the reaction between CH_3CHO and $^{\bullet}OH$ (eqn (20)). $^{\bullet}CH_3$ generated in eqn (18) and (20) could combine with $^{\bullet}OH$ into CH_3OH (eqn (21)).

$$CH_3CH_2OH + {}^{\bullet}OH \rightarrow {}^{\bullet}CH_3 + CH_2(OH)_2 \tag{18}$$

$$CH_2(OH)_2 + 2{}^{\bullet}OH \rightarrow HCOOH + 2H_2O \tag{19}$$

$$CH_3CHO + {}^{\bullet}OH \rightarrow {}^{\bullet}CH_3 + HCOOH \tag{20}$$

$${}^{\bullet}CH_3 + {}^{\bullet}OH \rightarrow CH_3OH \tag{21}$$
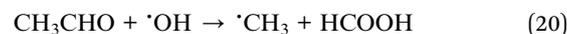
As-produced HCOOH could be decomposed into CO (eqn (22)) or further oxidized into CO_2 by $^{\bullet}OH$ (eqn (23)).

$$HCOOH \rightarrow CO + H_2O \tag{22}$$
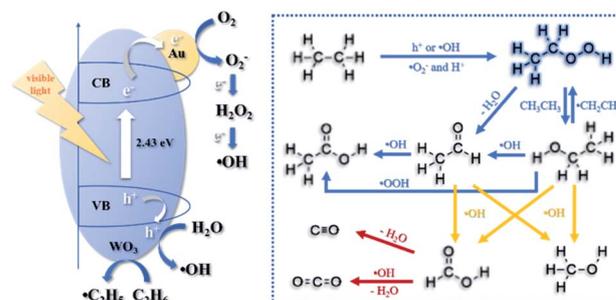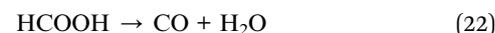
Fig. 5 Schematic reaction pathway for visible-light driven photocatalytic ethane oxidation over Au/WO_3.

$$HCOOH + 2^{\cdot}OH \rightarrow CO_2 + 2H_2O \qquad (23)$$
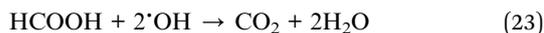
The reaction pathway was depicted in Fig. 5 based on above discussions. It should be noted that the reactions took place at the interface of Au and WO_3 for relieving the limitation of mass transfer. Moreover, it could be easily observed that $^{\cdot}OH$ was mainly responsible for further conversion of CH_3CH_2OOH. The high selectivity for CH_3CH_2OOH here was owed to its fast desorption from the catalyst surface due to the solvation effect of water and the elevated temperature to 100 °C, which suppressed its further oxidation. This provides a guidance to develop more efficient photocatalytic processes for the production of CH_3CH_2OOH.

Conclusions

In summary, highly efficient visible-light driven photocatalytic ethane conversion into a radical reservoir (namely, CH_3CH_2-OOH) was achieved over our created Au/WO_3 catalyst. The yield of CH_3CH_2OOH obtained at room temperature in two hours was as high as 1887 $\mu mol\ g_{cat}^{-1}$, which was further enhanced by six times by simply elevating the temperature to 100 °C. Moreover, a significant apparent quantum efficiency of 17.9% was obtained at 450 nm. Such a promotion was owed to the compensation effect of the kinetic energy of the reactants with regards to the insufficient potential energy in photocatalytic ethane oxidation over the narrow-band-gap Au/WO_3 catalyst. Furthermore, the reaction pathway was revealed by converting intermediate substances, trapping active species, and labeling reactants with isotopes, implying that $^{\cdot}OH$ plays a key role to determine the selectivity and activity of CH_3CH_2OOH production. Here, the excellent catalytic performance and the thorough analysis of the reaction mechanism will pave the way for scalable ethane conversion into CH_3CH_2OOH, which shows a great promise for cancer therapy by regulating the oxidative stress.

Experimental

Materials

Monoclinic WO_3 (99.8%, Macklin), P25 (99.5%, Sigma-Aldrich), ZnO (99.9%, Macklin), Bi_2O_3 (99.99%, Macklin), MoO_3 (99.50%, Alfa Aesar), and CeO_2 (99.99%, Macklin) were acquired to synthesize the catalysts. Freshly prepared 2 mg mL^{-1} $HAuCl_4$ (Sigma-Aldrich) aqueous solution was used as Au precursor. Other metal precursors included H_2PtCl_6 (Sigma-Aldrich), $PdCl_2$ (Sigma-Aldrich), $RhCl_3$ (Alfa Aesar), $AgNO_3$ (Sinopharm), $Cu(NO_3)_2$ (Sinopharm), and $Fe(NO_3)_3$ (Sinopharm). The free radical scavengers, p-benzoquinone (97%), EDTA–2Na (AR), and tertiary butyl alcohol (AR), were obtained from Macklin Co., Ltd. Feed gases, ethane (80% ethane + 20% nitrogen) and oxygen (99.99%), were supplied by Air Liquid Co., Ltd.

Catalyst preparation

Au was loaded on WO_3 via photo-deposition. Namely, 0.2000 g WO_3 was added into 40 mL deionized water to form a 5 g L^{-1} suspension, followed by adding 100 μL freshly prepared 20 mg mL^{-1} $HAuCl_4$ solution during vigorous stirring at 500 rpm (the theoretical Au loading amount: 1 wt%). The mixture was continuously stirred at 500 rpm for 20 min and then ultrasonicated for 20 min. Afterwards, the suspension was irradiated by an ultraviolet lamp (100 W, λ <400 nm) for 10 min while being stirred at 600 rpm. In this process, the color of the suspension was found to change from yellow to purple, demonstrating the reduction of Au^{3+}. The as-obtained Au/WO_3 suspension was washed and then collected via suction filtration with a 45 μm filter membrane. Lastly, the collected powder was dried at 60 °C for 12 h. Au/WO_3 catalysts with 0.1, 0.5, and 1.5 wt% Au were also prepared, with 10, 50, and 150 μL $HAuCl_4$ solutions, respectively. The real loading amount was confirmed by inductively coupled plasma mass spectrometry (ICP-MS).

In addition, Au was also loaded on commercial TiO_2, ZnO, Bi_2O_3, MoO_3, and CeO_2 as control samples, using the same method as above-described. Moreover, to investigate the influence of different metal cocatalysts, Pt, Pd, Ag, and Rh were photo-deposited on WO_3 with H_2PtCl_6, $PdCl_2$, $AgNO_3$, and $RhCl_3$ as the precursors, while Fe and Cu were loaded on WO_3 via impregnation and subsequent calcination at 400 °C for 6 h.

Catalyst characterization

X-ray diffraction (XRD) patterns were obtained from Shimadzu X-ray diffractometer (XRD-6100). The structures and morphologies of the catalysts were characterized using a FEI Tecnai G2 F20 field-emission transmission electron microscope (TEM) at an accelerating voltage of 200 kV. Attached energy dispersive X-ray spectroscopy (EDS) was employed for elemental analysis of the as-synthesized samples. The surface areas of the samples were measured and calculated using the multipoint Brunauer–Emmett–Teller (BET) technique with a BET Sorptometer (ASAP 2020 PLUS HD88) based on the adsorption isotherms. The chemical state and composition of the catalyst surface were determined via an X-ray photoelectron spectroscopy (XPS) instrument (Thermo EscaLab 250Xi). The element contents were measured by inductively coupled plasma mass spectrometry (ICP-MS) (Thermo iCAP Q). Ultraviolet-visible (UV-vis) absorption spectra of the catalysts were obtained using an UV-vis spectrometer (Shimadzu UV-2600). ^1H nuclear magnetic resonance (NMR) was conducted on a Bruker AVANCE III HD 400 NMR spectrometer using the liquid mixture obtained from ethane oxidation with deuterated water (D_2O).

DFT calculations

DFT calculations were conducted using Gaussian 16 package.[57] The geometric structure of the complex which contains one organic molecule (i.e., CH_3CH_2OOH or CH_3CH_2OH) and two water molecules was optimized using the B3LYP method[58] combined with the 6-311G(d,p) basis set.[59] The optimized structures were confirmed to be stable by frequency calculations. Afterwards, ^1H NMR chemical shifts were computed by the gauge-independent atomic orbital (GIAO) model[60] at the B3LYP/6-311++G(d,p) level,[58,61] using the self-consistent reaction field (SCRF)[62] technique in simulated water continuum.

The geometric structure and NMR shifts of the reference tetramethylsilane (TMS) were calculated using the same method.

Photocatalytic activity test

As shown in Fig. S6,† photocatalytic ethane oxidation was carried out in a 100 mL sealed stainless steel reactor with a concentric quartz window on the top. A 300 W xenon lamp (CEL-HXF300, AULIGHT) equipped with an UVcut420 filter, as the light source (λ >420 nm), was placed right above the reactor with the light intensity kept at 100 mW cm^{-2}. AM1.5G filter was employed to simulate the sunlight irradiation in some cases. In a typical test, 20 mg Au/WO$_3$ and 20 mL deionized water were added into the Teflon vessel, after which the reactor was vacuumed and purged with the C$_2$H$_6$/N$_2$ mixture gas for three times to remove any impurities in the system. Subsequently, 1.0 MPa C$_2$H$_6$/N$_2$ mixture (4 : 1) and 1.5 MPa O$_2$ were injected into the reactor. The photocatalytic reaction then started under visible light irradiation (λ >420 nm) at a certain temperature in the range of 35–200 °C during continuous stirring at 900 rpm. After reacting for 2 h, the reactor was placed in an ice bath for 30 min to ensure the termination of the reaction, and then as-produced CO and CO$_2$ were measured by a gas chromatograph (GC) (Fuli-9800) equipped with a TDX-01 packed column and a thermal conductive detector (TCD) working at 80 and 100 °C, respectively. Afterwards, the suspension was filtered, and the liquid was collected for product detection. CH$_3$CH$_2$OH, CH$_3$CHO, and CH$_3$OH were analyzed by GC with a Porapak Q column and a flame ionization detector (FID) by injecting 1 μL liquid. The temperatures of the injector, column, and FID detector were 150, 120, and 150 °C, respectively. CH$_3$CH$_2$OOH, CH$_3$COOH, and HCOOH were quantified by a high-performance liquid chromatograph (HPLC) (Shimadzu Essentia LC-16) with a C18 column (Φ 4.6 mm × 250 m) working at 35 °C.

The apparent quantum efficiency (AQE) was measured using a band-pass filter of monochromatic light of 450 nm ($\lambda_{1/2} = \sim$20 nm) at 100 °C following the same procedure as above described. All the products after two-hour reaction were quantified, and then the AQE was calculated *via* the following equations:

$$AQE = \frac{N(\text{photo generated electrons})}{N(\text{incident photons})} \quad (24)$$

$$N(\text{incident photons}) = \frac{I \times A \times \lambda}{h \times c} \times t \quad (25)$$

$$\begin{aligned} N(\text{photo generated electrons}) &= 2 \times N(CH_3CH_2OOH) + 2 \\ &\times N(C_2H_5OH) + 4 \times N(CH_3CHO) + 6 \times N(CH_3COOH) \\ &+ N(CH_3OH) + 5 \times N(HCOOH) + 5 \times N(CO) \\ &+ 7 \times N(CO_2) \end{aligned} \quad (26)$$

where I, A, λ, and t are light intensity, irradiation area, light wavelength, and duration, respectively, while h and c represent Planck's constant and light speed, respectively.

Furthermore, to identify the role of free radicals in photocatalytic ethane oxidation, 10 mM free radical scavenger, *i.e.*, *p*-benzoquinone (*p*-BQ), tertiary butyl alcohol (TBA), and ethylenediaminetetraacetic acid disodium salt dihydrate (EDTA–

2Na), was added into the catalyst suspension for photocatalytic activity test at 50 °C to avoid the decomposition of scavengers at high temperatures.

Isotope labeling experiment

Isotope labeling experiments were conducted simply by replacing general O$_2$ and H$_2$O with O$^{18}_2$, H$_2$O^{18}, or D$_2$O. The reaction temperature was controlled at 100 °C. The products were analyzed by gas chromatography-mass spectrometry (GC-MS) (Shimadzu QP 2020 NX) equipped with an RTX-WAX column and an electron ionization source working at 70 eV. The temperatures of the split injector, column, connector, and ionization source were set as 120, 40, 120, and 200 °C, respectively.

Electrochemical measurement

The photocurrent–time (i–t) curve and linear sweep voltammetry (LSV) curve were recorded for Au/WO$_3$ and WO$_3$ in a three-electrode cell with a 0.5 M Na$_2$SO$_4$ electrolyte under visible light irradiation. A fluorine-doped tin oxide glass coated with catalyst, Pt, and saturated Ag/AgCl performed as the working, counter, and reference electrodes, respectively. LSV measurement was preformed from 1.2 to 0.3 V (*vs.* SHE) at a sweep rate of 0.5 mV s^{-1}. Mott–Schottky analysis was carried out at 500, 1000, 1500, and 2000 Hz in the same cell in dark.

Author contributions

Conceptualization, YHH; methodology, YHH; investigation, YZ, SF, SC, YT, CW and YHH; formal analysis, YZ, SF, and YHH; writing – original draft, SF; writing – review & editing, YHH; supervision, YHH.

Conflicts of interest

There are no conflicts to declare.

Notes and references

1 K. Wada, K. Yoshida, T. Takatani and Y. Watanabe, *Appl. Catal., A*, 1993, **99**, 21–36.
2 Y. Zhu, S. Shi, C. Wang and Y. H. Hu, *Int. J. Energy Res.*, 2020, **44**, 708–717.
3 M. M. Forde, R. D. Armstrong, C. Hammond, Q. He, R. L. Jenkins, S. A. Kondrat, N. Dimitratos, J. A. Lopez-Sanchez, S. H. Taylor, D. Willock, C. J. Kiely and G. J. Hutchings, *J. Am. Chem. Soc.*, 2013, **135**, 11087–11099.
4 R. Jin, M. Peng, A. Li, Y. Deng, Z. Jia, F. Huang, Y. Ling, F. Yang, H. Fu, J. Xie, X. Han, D. Xiao, Z. Jiang, H. Liu and D. Ma, *J. Am. Chem. Soc.*, 2019, **141**, 18921–18925.
5 F. Battin-Leclerc, O. Herbinet, P.-A. Glaude, R. Fournet, Z. Zhou, L. Deng, H. Guo, M. Xie and F. Qi, *Angew. Chem., Int. Ed.*, 2010, **49**, 3169–3172.
6 D. Chen, H. Jin, Z. Wang, L. Zhang and F. Qi, *J. Phys. Chem. A*, 2011, **115**, 602–611.

7 W. Chamulitrat, N. Takahashi and R. P. Mason, *J. Biol. Chem.*, 1989, **264**, 7889–7899.

8 B. Kalyanaraman, C. Mottley and R. P. Mason, *J. Biol. Chem.*, 1983, **258**, 3855–3858.

9 Z. Zhou, J. Song, L. Nie and X. Chen, *Chem. Soc. Rev.*, 2016, **45**, 6597–6626.

10 Z. Zhou, J. Song, R. Tian, Z. Yang, G. Yu, L. Lin, G. Zhang, W. Fan, F. Zhang, G. Niu, L. Nie and X. Chen, *Angew. Chem., Int. Ed.*, 2017, **56**, 6492–6496.

11 A. Caputo, M. Brunori and R. Giuliano, *Cancer Res.*, 1961, **21**, 1499.

12 Y. Wan, G. Lu, J. Zhang, Z. Wang, X. Li, R. Chen, X. Cui, Z. Huang, Y. Xiao, J. Chelora, W. Zhang, Y. Liu, M. Li, H.-Y. Xie and C.-S. Lee, *Adv. Funct. Mater.*, 2019, **29**, 1903436.

13 C. Wang, F. Cao, Y. Ruan, X. Jia, W. Zhen and X. Jiang, *Angew. Chem., Int. Ed.*, 2019, **58**, 9846–9850.

14 C. Gorrini, I. S. Harris and T. W. Mak, *Nat. Rev. Drug Discovery*, 2013, **12**, 931–947.

15 D. E. J. G. J. Dolmans, D. Fukumura and R. K. Jain, *Nat. Rev. Cancer*, 2003, **3**, 380–387.

16 A. Hu, J.-J. Guo, H. Pan and Z. Zuo, *Science*, 2018, **361**, 668.

17 G. Laudadio, Y. Deng, K. van der Wal, D. Ravelli, M. Nuño, M. Fagnoni, D. Guthrie, Y. Sun and T. Noël, *Science*, 2020, **369**, 92–96.

18 C. T. Brigden, S. Poulston, M. V. Twigg, A. P. Walker and A. J. J. Wilkins, *Appl. Catal., B*, 2001, **32**, 63–71.

19 K. Wada, K. Yoshida, Y. Watanabe and T. Suzuki, *Appl. Catal.*, 1991, **74**, L1–L4.

20 M. Somekh, A. M. Khenkin, A. Herman and R. Neumann, *ACS Catal.*, 2019, **9**, 8819–8824.

21 K. Wada, H. Yamada, Y. Watanabe and T.-a. Mitsudo, *J. Chem. Soc., Faraday Trans.*, 1998, **94**, 1771–1778.

22 A. Tóth, T. Bánsági and F. Solymosi, *Mol. Catal.*, 2017, **440**, 19–24.

23 X. Wang, Z. He, S. Zhong and X. Xiao, *J. Nat. Gas Chem.*, 2007, **16**, 173–178.

24 X.-T. Wang, S.-H. Zhong and X.-F. Xiao, *J. Mol. Catal. A: Chem.*, 2005, **229**, 87–93.

25 R. Zhang, H. Wang, S. Tang, C. Liu, F. Dong, H. Yue and B. Liang, *ACS Catal.*, 2018, **8**, 9280–9286.

26 N. Djeghri, M. Formenti, F. Juillet and S. Teichner, *Faraday Discuss. Chem. Soc.*, 1974, **58**, 185–193.

27 M. P. Thekaekara, *Sol. Energy*, 1976, **18**, 309–325.

28 D. M. Schultz and T. P. Yoon, *Science*, 2014, **343**, 1239176.

29 R. Abe, H. Takami, N. Murakami and B. Ohtani, *J. Am. Chem. Soc.*, 2008, **130**, 7780–7781.

30 D. P. DePuccio, P. Botella, B. O'Rourke and C. C. Landry, *ACS Appl. Mater. Interfaces*, 2015, **7**, 1987–1996.

31 P. Y. Dong, G. H. Hou, X. U. Xi, R. Shao and F. Dong, *Environ. Sci.: Nano*, 2017, **4**, 539–557.

32 L. Chen and S. C. Tsang, *Sens. Actuators, B*, 2003, **89**, 68–75.

33 K. Wenderich, A. Klaassen, I. Siretanu, F. Mugele and G. Mul, *Angew. Chem., Int. Ed.*, 2014, **53**, 12476–12479.

34 C. A. Bignozzi, S. Caramori, V. Cristino, R. Argazzi, L. Meda and A. Tacca, *Chem. Soc. Rev.*, 2013, **42**, 2228–2246.

35 T. Zhu, M. N. Chong and E. S. Chan, *ChemSusChem*, 2014, **7**, 2974–2997.

36 X. Chen, L. Liu, P. Y. Yu and S. S. Mao, *Science*, 2011, **331**, 746.

37 B. Han and Y. H. Hu, *J. Phys. Chem. C*, 2015, **119**, 18927–18934.

38 S. Fang, Z. Sun and Y. H. Hu, *ACS Catal.*, 2019, **9**, 5047–5056.

39 S. Fang, Y. Liu, Z. Sun, J. Lang, C. Bao and Y. H. Hu, *Appl. Catal., B*, 2020, **278**, 119316.

40 B. Han, W. Wei, L. Chang, P. Cheng and Y. H. Hu, *ACS Catal.*, 2016, **6**, 494–497.

41 B. Han, W. Wei, M. Li, K. Sun and Y. H. Hu, *Chem. Commun.*, 2019, **55**, 7816–7819.

42 X. Wu, J. Lang, Y. Jiang, Y. Lin and Y. H. Hu, *ACS Sustainable Chem. Eng.*, 2019, **7**, 19277–19285.

43 C. Wang, S. Fang, S. Xie, Y. Zheng and Y. H. Hu, *J. Mater. Chem. A*, 2020, **8**, 7390–7394.

44 F. Sastre, A. Corma and H. García, *Appl. Catal., B*, 2012, **128**, 84–90.

45 Q. Li, H. Yue, C. Liu, K. Ma, S. Zhong, B. Liang and S. Tang, *Chem. Eng. J.*, 2020, **395**, 125120.

46 A. Tanaka, K. Hashimoto and H. Kominami, *J. Am. Chem. Soc.*, 2014, **136**, 586–589.

47 N. Minh Vuong, D. Kim and H. Kim, *Sci. Rep.*, 2015, **5**, 11040.

48 Y. Wang, B. Zhang, J. Liu, Q. Yang, X. Cui, Y. Gao, X. Chuai, F. Liu, P. Sun, X. Liang, Y. Sun and G. Lu, *Sens. Actuators, B*, 2016, **236**, 67–76.

49 L. Wang, C.-S. Tsang, W. Liu, X. Zhang, K. Zhang, E. Ha, W.-M. Kwok, J. H. Park, L. Y. Suk Lee and K.-Y. Wong, *J. Mater. Chem. A*, 2019, **7**, 221–227.

50 W. He, H.-K. Kim, W. G. Wamer, D. Melka, J. H. Callahan and J.-J. Yin, *J. Am. Chem. Soc.*, 2014, **136**, 750–757.

51 P. Wardman, *J. Phys. Chem. Ref. Data*, 1989, **18**, 1637–1755.

52 Y. Nosaka and A. Y. Nosaka, *Chem. Rev.*, 2017, **117**, 11302–11336.

53 H. Li, Z. Bian, J. Zhu, Y. Huo, H. Li and Y. Lu, *J. Am. Chem. Soc.*, 2007, **129**, 4538–4539.

54 V. Jovic, W.-T. Chen, D. Sun-Waterhouse, M. G. Blackford, H. Idriss and G. I. N. Waterhouse, *J. Catal.*, 2013, **305**, 307–317.

55 H. Song, X. Meng, S. Wang, W. Zhou, X. Wang, T. Kako and J. Ye, *J. Am. Chem. Soc.*, 2019, **141**, 20507–20515.

56 X. Chen, Y. Li, X. Pan, D. Cortie, X. Huang and Z. Yi, *Nat. Commun.*, 2016, **7**, 12273.

57 M. Frisch, G. Trucks, H. Schlegel, G. Scuseria, M. Robb, J. Cheeseman, G. Scalmani, V. Barone, G. Petersson and H. Nakatsuji, *Gaussian 16*, 2016.

58 P. J. Stephens, F. J. Devlin, C. F. Chabalowski and M. J. Frisch, *J. Phys. Chem.*, 1994, **98**, 11623–11627.

59 P. C. Hariharan and J. A. Pople, *Theor. Chim. Acta*, 1973, **28**, 213–222.

60 K. Wolinski, J. F. Hinton and P. Pulay, *J. Am. Chem. Soc.*, 1990, **112**, 8251–8260.

61 K. Raghavachari and G. W. Trucks, *J. Chem. Phys.*, 1989, **91**, 1062–1065.

62 V. Barone, M. Cossi and J. Tomasi, *J. Chem. Phys.*, 1997, **107**, 3210–3221.